Journal of
Composites Science

MDPI

Article

Investigation of the Characteristics of MAO Coatings Formed on Ti6Al4V Titanium Alloy in Electrolytes with Graphene Oxide Additives

Sergey Grigoriev [1], Nikita Peretyagin [1,2,*], Andrey Apelfeld [3], Anton Smirnov [1,*], Alevtina Rybkina [4], Ekaterina Kameneva [5], Artem Zheltukhin [1], Mikhail Gerasimov [6], Marina Volosova [1], Oleg Yanushevich [2], Natella Krikheli [2] and Pavel Peretyagin [1,2,*]

1 Spark Plasma Sintering Research Laboratory, Moscow State University of Technology "STANKIN", Vadkovsky per.1, Moscow 127055, Russia; s.grigoriev@stankin.ru (S.G.); artem.zheltuhin@mail.ru (A.Z.); m.volosova@stankin.ru (M.V.)
2 Scientific Department, A.I. Evdokimov Moscow State University of Medicine and Dentistry, Delegatskaya St., 20, p.1, Moscow 127473, Russia; olegyanushevich@mail.ru (O.Y.); nataly0088@mail.ru (N.K.)
3 Department 1203, Moscow Aviation Institute National Research University, Volokolamskoe Shosse, 4, Moscow 125993, Russia; apelfeld@yandex.ru
4 Laboratory of Corrosion of Metals in Natural Conditions, Institute of Physical Chemistry and Electrochemistry of RAS, Leninsky Prospect, 31, k.4, Moscow 119071, Russia; aa_rybkina@mail.ru
5 Department of Physical and Quantum Electronics, Moscow Institute of Physics and Technology (National Research University), Institutskiy per., 9, Dolgoprudny, Moscow 141701, Russia; katerinakamenev@yandex.ru
6 Laboratory of Oxidation and Passivation of Metals and Alloys, Institute of Physical Chemistry and Electrochemistry of RAS, Leninsky Prospect, 31, k.4, Moscow 119071, Russia; mvger2018@yandex.ru
* Correspondence: n.peretyagin@stankin.ru (N.P.); a.smirnov@stankin.ru (A.S.); p.peretyagin@stankin.ru (P.P.); Tel.: +7-4999-7323-70 (N.P.)

check for updates

Citation: Grigoriev, S.; Peretyagin, N.; Apelfeld, A.; Smirnov, A.; Rybkina, A.; Kameneva, E.; Zheltukhin, A.; Gerasimov, M.; Volosova, M.; Yanushevich, O.; et al. Investigation of the Characteristics of MAO Coatings Formed on Ti6Al4V Titanium Alloy in Electrolytes with Graphene Oxide Additives. *J. Compos. Sci.* **2023**, *7*, 142. https://doi.org/10.3390/jcs7040142

Academic Editor: Prashanth Konda Gokuldoss

Received: 1 March 2023
Revised: 23 March 2023
Accepted: 31 March 2023
Published: 6 April 2023

Abstract: Coatings with a thickness from ~40 to ~50 µm on Ti6Al4V titanium alloy were formed by micro-arc oxidation in a silicate-hypophosphite electrolyte with additions of graphene oxide. Micro-arc oxidation treatment was carried out in the anode–cathode mode (50 Hz) with a ratio of anode to cathode currents of 1:1, a total density of 20 A/dm^2, and a treatment duration of 30 min. The effect of the graphene oxide concentration in electrolytes on the thickness, roughness, hardness, surface morphology, structure, composition of micro-arc oxidation coatings, and its electrochemical corrosion behavior in 3.5% NaCl solution was studied. The input of graphene oxide additives into the base silicate hypophosphite electrolyte led to an increase in the hardness of micro-arc oxidation coatings. Electrochemical polarization studies and impedance data showed that the best characteristics in terms of corrosion-protective ability among coatings formed in electrolytes with graphene oxide additives were those formed in the electrolyte with a graphene oxide concentration of 0.1 g·L^{-1}. A further increase in the graphene oxide concentration in the electrolyte did not improve the protective properties of micro-arc oxidation coatings.

Keywords: titanium alloy Ti6Al4V; micro-arc oxidation; graphene oxide; MAO coating; thickness; roughness; hardness; surface morphology; structure; composition; electrochemical polarization curves; electrochemical impedance spectroscopy

1. Introduction

At present, the surface modification of titanium and, in particular, Ti6Al4V alloy, which shows low density, high strength, fatigue resistance, and biocompatibility [1–4], has found application in various industries (marine, automotive, aerospace, chemical, and biomedical) [5–7]. Among various methods of modifying the surface of light alloys, i.e., CVD, PVD, and thermal oxidation [8–10], the drawbacks of which are presented in studies [11,12], micro-arc oxidation (MAO) is of particular interest because it has advantages

over other methods such as processing cost, versatility, ease of operation, and environmental friendliness [13–15]. A particularly important feature of MAO is the flexibility in selecting electrolyte compositions, which makes it possible to obtain oxide layers with different properties [16–18]. Due to the electrochemical nature of the oxide layers formed in the MAO process, the characteristics of the electrolytes used, including conductivity, acidity, chemical composition, and types of additives, can significantly influence the properties of the deposited coatings, such as morphology, porosity, and surface phase composition [19–21]. Therefore, the incorporation of additives with micro- and nano-sized particles into the formed layer can be an important strategy to improve the properties of coatings and expand the range of chemical composition. Various electrolytes containing compounds such as alumina [22], copper oxide [23], zirconia [24], graphene [25], and graphene oxide (GO) [26] are used to impart special properties to MAO coatings on titanium alloys [27–31]. Of all the presented additives, GO is of greatest interest due to its ability to form stable dispersions in water and organic solvents, as it contains on the surface various functional groups (carboxyl, hydroxyl, phenolic, epoxy, etc.). These groups are easily formed during the oxidation of graphene in a strongly acidic environment, and, in aqueous solutions, can participate in ion exchange processes [32–34]. Chen et al. [25] obtained ceramic coatings with different concentrations of graphene particles on 6063 Al alloy substrates by the MAO method in an electrolyte containing sodium metasilicate (Na_2SiO_3), sodium fluoride (NaF), trisodium phosphate (Na_3PO_4), and sodium hydroxide (NaOH) and concluded that the best mechanical and corrosion properties were obtained at a graphene particle concentration of 0.15 g/L. Gao et al. [26] investigated the effect of MAO of a pure titanium substrate when 100 mg/L of graphene oxide and 2 g/L of sodium dodecyl benzene sulfonate were added to the aqueous solution of sodium silicate ($Na_2SiO_3 \cdot 9H_2O$, 20 g/L). To fabricate TiO_2 ceramic coatings, the constant-voltage mode was selected and 450 V was predefined. The MAO parameters were as follows: frequency 500 Hz, duty cycle 6%, and time 5 min. The results showed that the obtained composite coatings have improved photocatalytic activity, enhanced binding force, and excellent corrosion resistance. Wen et al. [27] synthesized a MAO bioactive hydroxyapatite (HA) with 1 wt.% GO on a magnesium alloy substrate in a phosphate electrolyte and found that HA/GO particles were successfully incorporated into the composite coating, the number and diameter of pores in the coating decreased, the corrosion current density of the HA/GO-coated sample decreased to 36.43 $\mu A/cm^2$ compared to the Mg substrate (2124 $\mu A/cm^2$) in simulated body fluid solution, and the polarization resistance of the HA/GO-coated sample increased significantly, indicating that the HA/GO coating can provide a more effective barrier against corrosion ion penetration than the MAO coating. Li et al. [28] obtained GO-containing coatings on Zr N36 alloy by the MAO method. The oxidation in this work was performed in two electrolytes containing Na_2SiO_3/NaF/potassium hydroxide KOH and Na_2SiO_3/Na_3PO_4/NaF/KOH. The GO content ranged from 0 g/L to 0.1 g/L. The conclusions of their studies were that GO did not change the phase composition of the coatings, and GO-containing coatings showed a lower self-corrosion current density, more positive corrosion potential, and increased fretting wear. Zhang et al. [29] investigated a ceramic MAO-coating, with GO sheets embedded in it, on an Mg-Li alloy substrate. The base electrolyte consisted of Na_2SiO_3 and KOH, with GO (10 mL/L) added to it. This resulted in ~60 µm thick coatings with reduced roughness and porosity compared to those without GO. The addition of GO improved the hardness as well as scratch resistance, and the GO-containing coatings also exhibited excellent anti-friction and anti-wear properties. Askarnia et al. [30] applied the MAO process to AZ91 magnesium alloy in an alkaline electrolyte with different GO contents (0, 10, 20, and 30 mg/L). The coating with a GO concentration of 20 mg/L was characterized as optimal in surface quality as well as in mechanical and corrosion properties. In addition, antibacterial studies showed that coatings with 30 mg/L showed the best properties. Wang et al. [31] performed surface layer modification on Ti-3Zr-2Sn-3Mo-25Nb titanium alloy by the MAO method at pulsed direct current in an electrolyte containing 4.1 g/L of potassium dihydrogen phosphate, 19.62 g/L of calcium acetate, 21.94 g/L of EDTA-2Na stabilizer, and 5 mg/L of graphene

oxide. The results showed that compared with the original MAO coating, GO added into the system led to a more uniform surface, some pores were sealed, and the surface roughness was reduced. After doping with GO, the overall thickness of the coating decreased from ~50 to ~40 μm but the hardness increased from ~290 to ~310 HV, and the friction coefficient was reduced by 50%. Electrochemical testing showed GO had an enhancing effect on the corrosion resistance of the MAO coating. In [13], interesting results were obtained on the thermal stability of coatings formed in a silicate-hypophosphite electrolyte in the anode–cathode (50 Hz) MAO mode on the samples made by the method of electron beam melting using additive technology from Ti6Al4V titanium alloy powder.

The aim of this work is to study the effect of GO additives in a silicate-hypophosphite electrolyte on the characteristics (hardness, electrochemical, corrosion behavior, etc.) of MAO coatings formed on a compact Ti6Al4V titanium alloy.

2. Materials and Methods

In this study, commercial graphite powder (Plasmotherm, Moscow, Russia) with a median particle size d_{50} = 3 μm and carbon content ≥99.99% was used. The Raman spectrum and SEM image of raw graphite powder are presented in Figure 1. Graphite platelets have the form of flakes or a layered morphology. The Raman spectrum of the graphite powder demonstrates the characteristic peaks located at ~1584 cm^{-1} (G) and it is more intense than the 2D (2720 cm^{-1}) and D (1350 cm^{-1}) bands.

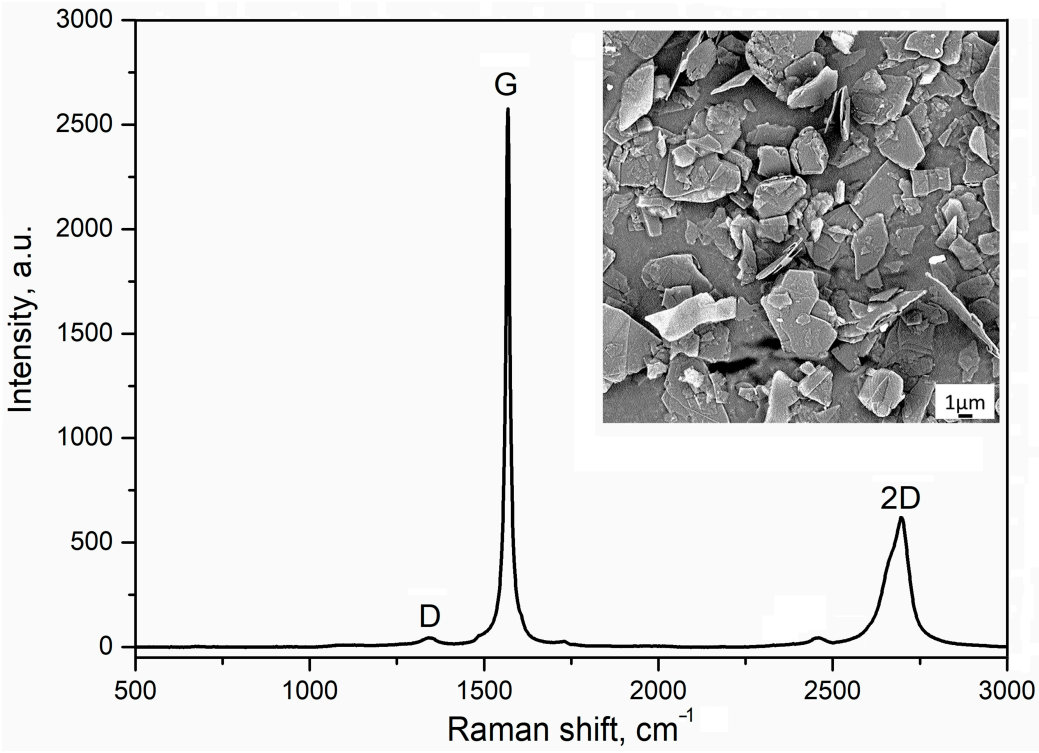

Figure 1. Raman spectrum and SEM image of raw graphite powder.

A modified Hummers method was used to obtain graphene oxide from graphite powder (Figure 2).

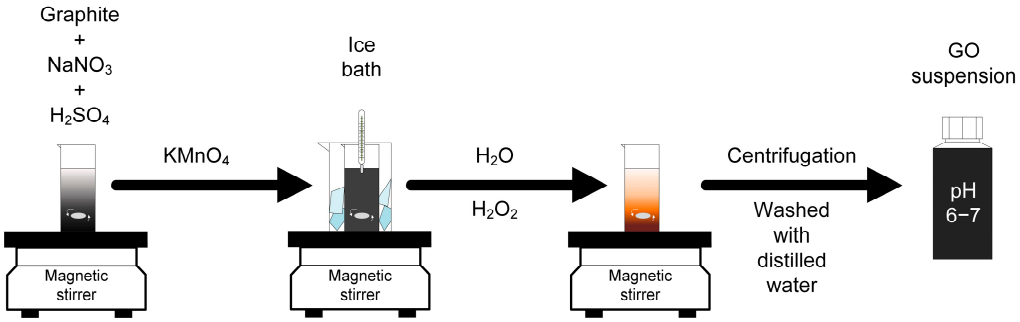

Figure 2. Schematic illustration of the modified Hummers method for synthesis of graphene oxide.

Concentrated sulfuric acid was added to a mixture of commercial graphite and nitric acid while stirring in a thin stream for this purpose. The resulting solution was cooled in an ice bath with constant stirring to T = 0–10 °C with a holding time of 25 min. Then, under continuous stirring and constant cooling, potassium permanganate was added in small portions with the reaction temperature control no more than 20 °C. The next step was to heat the solution to 35 °C and stir for 3 h. Upon completion of the reaction, the suspension acquired a dough-like structure and a dark brown color. After that, purified water was slowly added to avoid the release of large amounts of heat. To reduce the residual potassium permanganate and manganese oxide to colorless manganese sulphate, a 3% hydrogen peroxide solution was slowly added, resulting in a pronounced exothermic effect up to 98 °C and a color change of the solution to a dark yellow-brown. The reaction mixture was stirred for 30 min and centrifuged (3700 rpm for 30 min). The remaining solid material was washed with distilled water and centrifuged again until a neutral pH of the solution (pH ~6–7) was reached [33,34]. MAO coatings were formed on disc samples with a diameter of 27 mm and thickness of 7 mm made of the Ti6Al4V alloy (Lkalloy, Shanghai, China, structure and chemical composition presented in Table 1). The samples with a surface roughness equal to Ra = 1.8 μm and Rz = 11.5 μm were degreased with acetone for 25 min in an ultrasonic bath, washed with distilled water, and then were cleared by blowing pressurized air before post-mortem observations.

Table 1. Structure and chemical composition of Ti6Al4V alloy.

Structure	**Chemical Composition, wt.%**			
α + β	Al	V	Fe	Ti
	5.5−6.75	3.5−4.5	0.3	Bal.

MAO treatment was carried out in a silicate-hypophosphite base electrolyte comprising 10 $g \cdot L^{-1}$ of $Na_2SiO_3 \cdot 9H_2O$ and 5 $g \cdot L^{-1}$ of $Na(PH_2O_2) \cdot H_2O$, with additions of 0.1, 0.3, and 0.5 $g \cdot L^{-1}$ of graphene oxide. MAO treatment was carried out on an experimental setup in the anode–cathode mode (50 Hz), with an anode-to-cathode current ratio of 1:1 and sum current density of 20 A/dm^2. The duration of the MAO treatment was 30 min. The pH and conductivity of the electrolytes were measured using a pH meter and a conductometer (Mettler Toledo, Columbus, OH, USA). The electrolyte temperature was monitored in real-time using a resistance thermometer located in the zone of MAO treatment of the samples and was maintained in the range of 23–26 °C. During the MAO treatment, the electrolyte was stirred by bubbling with compressed air. To stabilize graphene oxide particles in the electrolytes used, they were pretreated for 20 min in a homogenizer with ultrasound at a frequency of 40 kHz. The sample code, composition of electrolytes, and their pH and conductivity are presented in Table 2.

Table 2. The sample code and main technological parameters of MAO process.

Samples Code	Base Electrolyte	Graphene Oxide Addition, $g \cdot L^{-1}$	pH	Conductivity, $mS \cdot cm^{-1}$
0 GO	$Na_2SiO_3 \cdot 9H_2O$ + $Na(PH_2O_2) \cdot H_2O$	0	12.25	31.23
0.1 GO		0.1	12.21	37.87
0.3 GO		0.3	12.12	41.34
0.5 GO		0.5	12.04	47.61

The surface morphology and cross-sectional structure of MAO coatings were studied using the scanning electron microscope (SEM) VEGA 3 LMH (Tescan, Brno, Czech Republic) equipped with an energy-dispersive X-ray spectrometer (EDS). Images were obtained at the accelerating voltage of 10 kV using a secondary electron detector (SE), which formed a topographic contrast. EDS was carried out at an accelerating voltage of 20 kV to activate all the main lines of the elements and the working distance of 15 mm. By EDS-analysis, the elemental composition of the studied areas and the distribution map of the elements were obtained. The thickness of MAO coatings was measured with the eddy current thickness gauge VT-201 (KID, Moscow, Russia). The roughness was measured using the optical system MicroCAD premium+ (GFM, Berlin, Germany). The microhardness of the MAO coatings was measured using a PMT-3M microhardness tester (LOMO, Saint Petersburg, Russia) with a load of 0.98 N g and a loading time of 10 s. X-ray phase analysis was carried out with Cu Kα radiation at a voltage of 30 kV and angles 2θ from 15 to 80 degrees on the diffractometer Difrey-401k (Scientific Instruments JSC, Saint Petersburg, Russia). Raman spectroscopy was performed on a DXR^{TM2} (Thermo Fisher Scientific, Waltham, MA, USA) using a 532 nm laser with a power of 2.0 mW for the characterization of the obtained coatings.

The electrochemical behavior of bare and coated samples was investigated in an NaCl solution with a concentration 3.5%, which is typical for such studies [26,35]. The studies were carried out in the three-electrode cell with separated anodic and cathodic spaces using an IPC-Pro MF potentiostat (LLC Volta, Saint Petersburg, Russia) with potentiodynamic polarization from the cathode to the anode field with a sweep rate of 1 mV/s. The Ti6Al4V alloy substrate and coated samples were used as working electrodes, the silver chloride electrode (Ag/AgCl) as the reference electrode, and a platinum plate as the auxiliary electrode. Potentiodynamic polarization measurements were carried out at room temperature. Polarization measurements were started after 30 min of immersion in the corrosive solution. After this time, the steady-state open-circuit potential (OCP) corresponding to the corrosion potential of the working electrode was obtained. The potentials are reported versus the standard hydrogen electrode (SHE).

Electrochemical impedance spectroscopy (EIS) was carried out using the potentiostatic complex IPC-FRA (Moscow, Russia) [36] with a corrosion potential (open-circuit) with the superimposition of a sinusoidal alternating-current signal with an amplitude of 10 mV in the frequency range of 0.1 Hz . . . 10 kHz. The subsequent calculation of the parameters of the equivalent impedance scheme according to the program was carried out with reduction to S = 1 cm^2. The error bars for all electrochemical measurements in parallel experiments did not exceed 10%.

3. Results and Discussion

Table 2 shows that with an increase in the content of graphene oxide in the electrolyte from 0 to 0.5 $g \cdot L^{-1}$, its pH slightly decreases, while the conductivity of the electrolyte increases by about 1.5 times. This means that the voltage drop across the discharges increases, and this should intensify the MAO process.

Figure 3 shows SEM images of the surface morphology of MAO coatings formed in electrolytes with different contents of GO. It can be seen that with an increase in the concentration of graphene oxide, the open porosity of the coatings noticeably decreases, which should lead to an increase in their corrosion-protective ability.

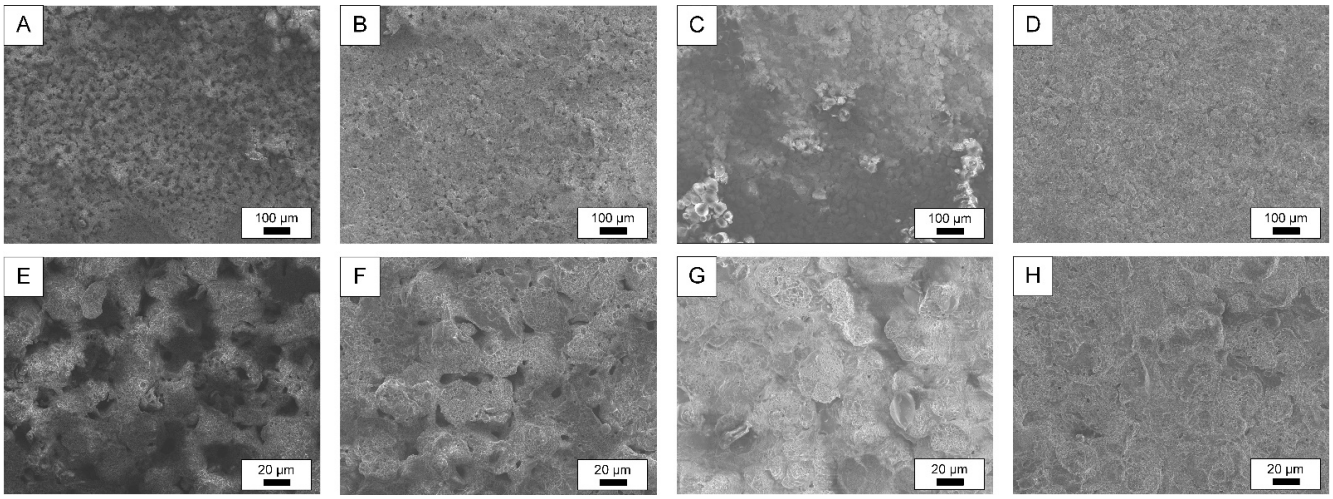

Figure 3. SEM images of the surface morphology of different MAO-coated samples: 0 GO (**A**,**E**), 0.1 GO (**B**,**F**), 0.3 GO (**C**,**G**), 0.5 GO (**D**,**H**).

Table 3 presents the results of measuring the thickness, roughness, and Vickers hardness of MAO coatings formed in electrolytes with different contents of graphene oxide.

Table 3. Thickness, roughness, and hardness (HV) of MAO coatings.

Sample Code	Thickness, µm	Roughness, µm		Hardness (HV)
		Ra	Rz	
Substrate		1.8	11.5	302
0 GO	40.9	3.3	19.2	317
0.1 GO	48.5	6.4	35.3	331
0.3 GO	48.7	6.9	37.8	352
0.5 GO	49.5	7.1	39.4	366

It can be seen that with an increase in the graphene oxide content in the electrolyte from 0 to 0.1 g·L^{-1}, the coating thickness increases by about 20%, and with a further increase in the GO concentration from 0.1 to 0.5 g·L^{-1}, a very slight increase in the coating thickness occurs. This may be due to the fact that excessive amounts of graphene oxide particles block discharge channels, which prevents an increase in the growth rate of coatings. Another explanation may be that an excess amount of GO coagulates in the electrolyte and does not participate in the formation of MAO coatings [36]. The surface roughness of the samples after oxidation in the GO-free electrolyte increases approximately doubles. Adding graphene oxide to the electrolyte leads to about the same effect as in the case of the coating thickness. Adding 0.1 g/L of GO to the electrolyte still increases the roughness by about double, but when the concentration of graphene oxide in the electrolyte is further increased, it almost does not increase. MAO treatment of the Ti6Al4V alloy in the base electrolyte increases its surface hardness by approximately 5% from 302 to 317 HV. Introducing GO to the electrolyte leads to an almost monotonic increase in hardness of MAO coatings from 331 to 366 HV with an increase in the GO concentration from 0.1 to 0.5 g·L^{-1}. Approximately such a hardness growth was found in work [36], in which an increase in the GO content in the electrolyte from 5 to 15 mL·L^{-1} led to a monotonic increase in the hardness of MAO coatings on the Ti6Al4V titanium alloy from 345 to 375 HV. It is known [37] that the interaction of titanium and carbon at ~2000 °C results in the formation of titanium carbide, and the temperature in microarc discharges can reach 2000–3000 °C [14]. Therefore, an increase in the hardness of coatings with an increase in the concentration of graphene oxide in the electrolyte can be explained by the synthesis in discharges during MAO of increasing amounts of titanium carbide TiC and the formation of a composite structure of coatings similar to hard alloys. It can be noted that there are no peaks of the TiC phase in

the X-ray diffraction patterns. This may be due to the small volume fraction of TiC or to the fact that the TiC phase can be in the amorphous state. The amorphization of the oxide layer is also indicated by the presence of a "halo" in the diffractograms at small angles 2θ (less than 30 degrees). It should also be noted that a decrease in the open porosity of the coatings can hardly lead to an increase in their hardness. The open porosity of the coatings decreases due to the fact that open pores in the process of micro-arc oxidation are filled with graphene oxide, including a partially reduced one, and they have a much lower hardness than titanium or silicon oxide, which form the basis of MAO coatings formed on alloy Ti6Al4V in the silicate-hypophosphite electrolyte.

The wettability is usually related to the surface separation energy and bonding process, and recent work [38] has reported that the functional composition would exert obvious influences on the density-of-states distribution, bonding states, and surface separation energy. This, in combination with the lubricating effect of graphene, which can be reduced from graphene oxide during cathodic half-cycles of the MAO mode, should lead to an increase in the wear resistance of MAO coatings.

Figures 4 and 5 show the SEM-EDS elemental distribution maps and the cross-sectional microstructure of the MAO coating as well as the element distribution along the marked line, respectively, for 0.5 GO samples.

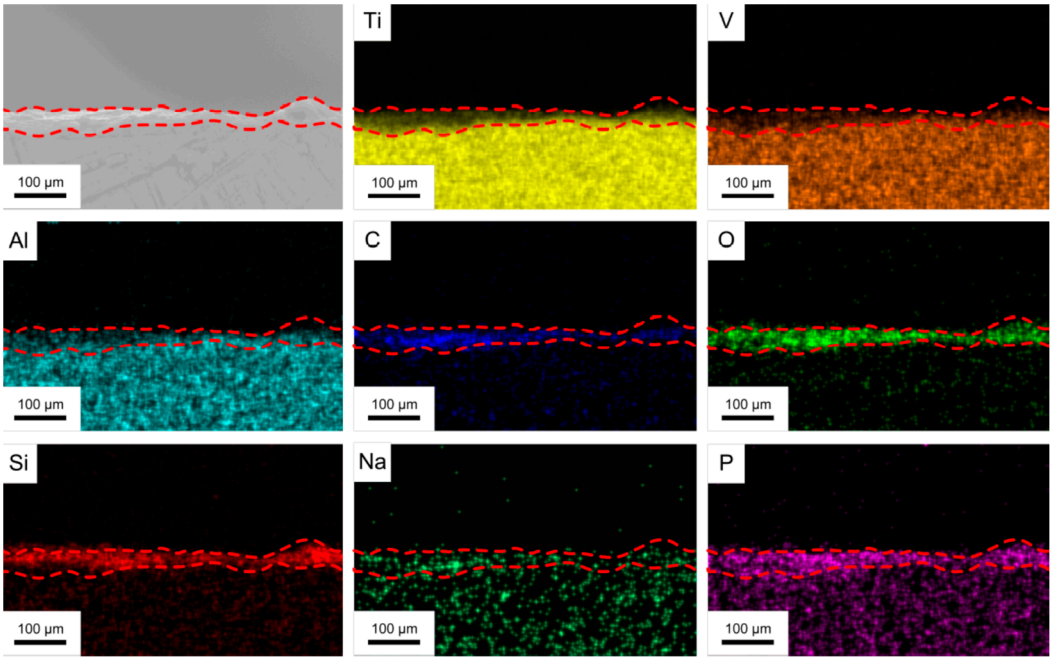

Figure 4. SEM-EDS elemental distribution maps for 0.5 GO MAO-coated sample. The coating is indicated by red dashed lines.

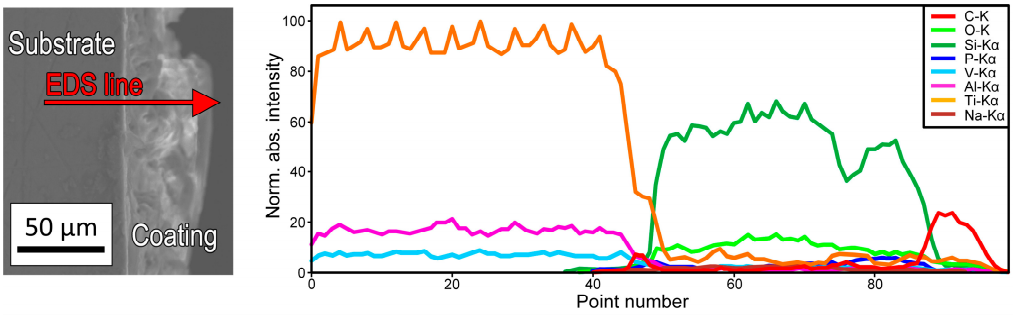

Figure 5. The cross-sectional microstructure of MAO coating (0.5 GO), and the element distribution along the marked line.

It can be seen that the carbon from graphene oxide, along with titanium and oxygen, alloying elements of the Ti6Al4V alloy (aluminum and vanadium), as well as elements of the electrolyte (silicon, phosphorus, and sodium), comprise the MAO coating. Figure 6 shows X-ray diffraction patterns of MAO coatings formed in electrolytes with different contents of graphene oxide. It can be seen that the height of the peaks of the high-temperature phase of titanium dioxide TiO_2-rutile (the temperature of the anatase-rutile polymorphic transformation is 620–650 °C) increases with an increase in the GO concentration in the electrolyte. This can be explained by the fact that at a higher concentration of graphene oxide, the electrolyte conductivity increases, and the discharge voltage and temperature in the discharge increase. It should be noted that anatase is observed only in thicker coatings formed in electrolytes containing graphene oxide. This may indicate the "immersion" of the high-temperature region of discharges deep into the pore channels of the MAO coating and insufficient heating of its surface layer.

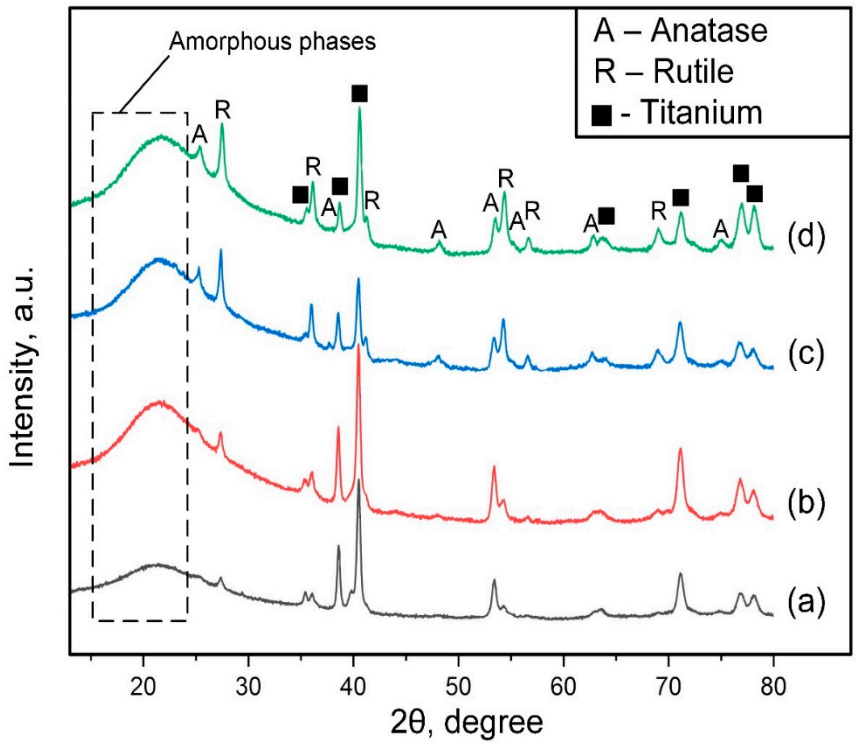

Figure 6. X-ray diffraction patterns of the 0 GO (**a**), 0.1 GO (**b**), 0.3 GO (**c**), and 0.5 GO (**d**) after MAO treatment.

It should also be noted that the X-ray diffraction patterns do not contain peaks of silicon-containing phases, such as silicon dioxide SiO_2 (α-cristobalite and α-quartz), titanosilicates, and aluminosilicates, with a significant amount of silicon itself in the MAO coating (Figure 4). This suggests that they are in an amorphous state. The amorphization of the oxide layer is also indicated by the presence of a "halo" in the diffractograms at small angles 2θ (less than 30 degrees).

The Raman spectra of the studied samples are shown in Figure 7. The peaks with abscissas of 1356 cm^{-1} and 1597 cm^{-1} correspond to the D and G peaks of graphene oxide, which indicates its presence in the MAO coatings on samples 0.1 GO, 0.3 GO, and 0.5 GO. The absence of enhancement of the D and G peaks with an increase in the concentration of graphene oxide in the electrolyte from 0.1 to 0.5 $g \cdot L^{-1}$ indicates that the content of GO in the oxide layers does not increase in this case. This may be due to the fact that an excess amount of graphene oxide coagulates in the electrolyte and does not participate in the formation of MAO coatings.

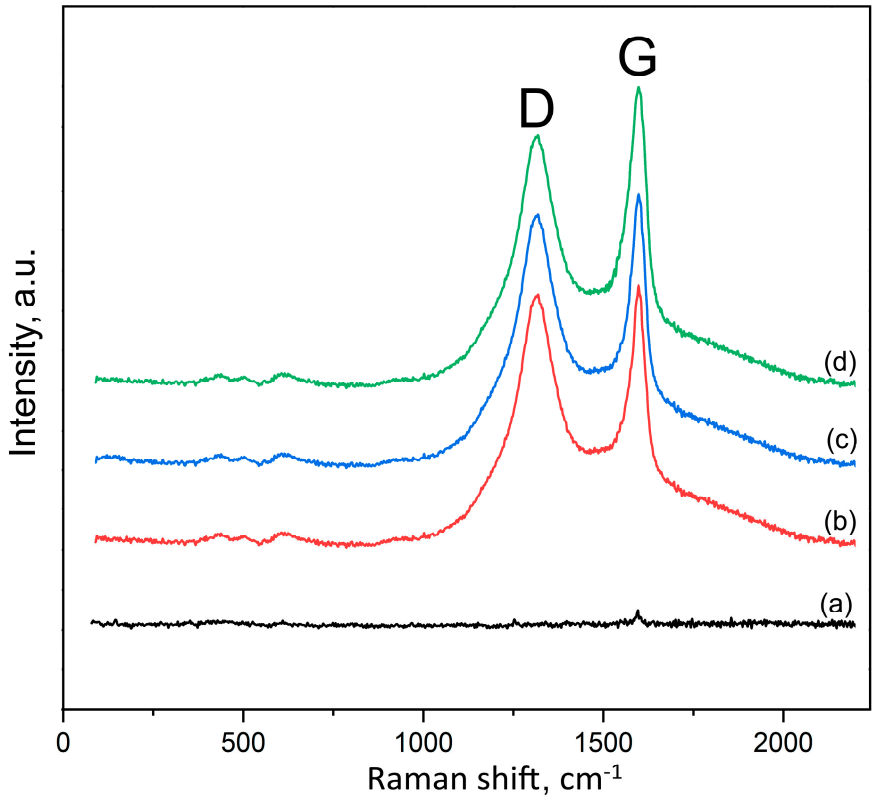

Figure 7. Raman spectra of the 0 GO (**a**), 0.1 GO (**b**), 0.3 GO (**c**), and 0.5 GO (**d**) samples after MAO treatment. "D" and "G" denote GO peaks.

Figure 8 shows the potentiodynamic polarization curves for the bare Ti6Al4V alloy (substrate) and samples with MAO coatings formed in electrolytes with different concentrations of graphene oxide.

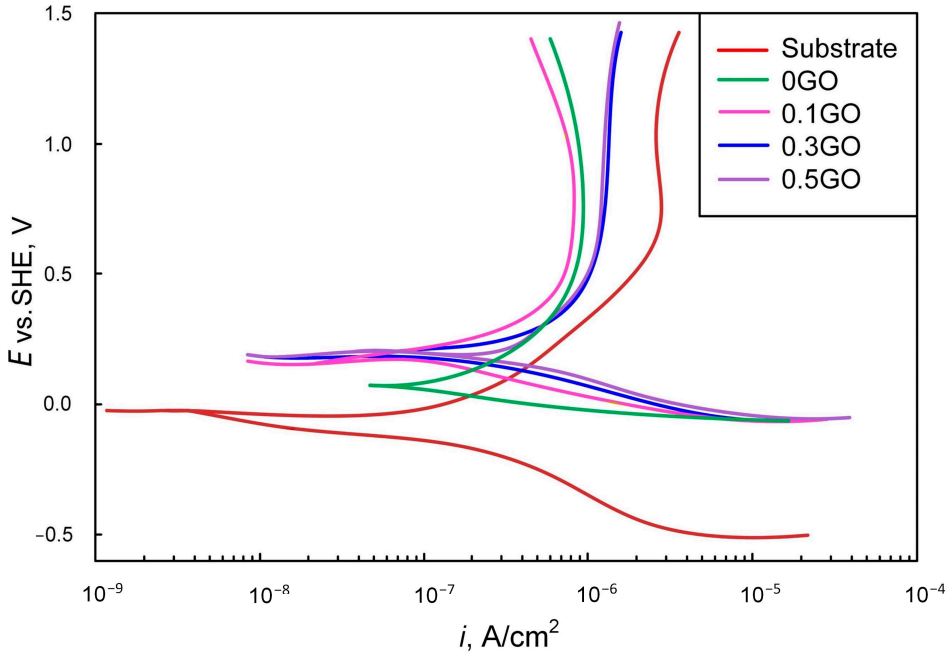

Figure 8. Potentiodynamic polarization curves after 30 min of immersion in corrosive solution of 3.5% NaCl at room temperature for all studied samples.

It can be seen that in this corrosive environment (3.5% NaCl) at room temperature, the Ti6Al4V titanium alloy is in a passive state. This is evidenced by the values of the corrosion potential E_{corr} and current densities on the anode branch of the polarization curve. During MAO treatment, thick oxide layers are formed on the alloy surface. This leads to a significant ennoblement of the corrosion potential, i.e., its shift in the positive direction by 150–250 mV compared to the bare alloy. In this case, the system enters the region of complete passivation with the values of the anode current densities of complete passivation i_{cp} corresponding to this state (Table 4). It can be assumed that when using MAO coatings in a more aggressive way for titanium than the 3.5% NaCl corrosive environment, their protective ability will also be high.

Table 4. Results of potentiodynamic polarization measurements; E_{corr}—corrosion potential (SHE); i_{cp}—anode current density of complete passivation at potential of 900 mV (SHE).

Sample Code	E_{corr}(SHE), mV	i_{cp}, A/cm^2
Substrate	−50	2.65×10^{-6}
0 GO	100	0.88×10^{-6}
0.1 GO	200	0.81×10^{-6}
0.3 GO	200	1.35×10^{-6}
0.5 GO	200	1.25×10^{-6}

Compared to the coating obtained in the base electrolyte, for MAO coatings formed in electrolytes with additives of graphene oxide, there is a shift in corrosion potentials by 100 mV toward more positive potential values (Table 4), i.e., into the area of deeper passivity. This is consistent with other studies, where a decrease in porosity and an increase in the density of coatings formed on titanium in electrolytes with additives of graphene oxide were noted [22]. The cathodic polarization curves for the 0.1 OG, 0.3 OG, and 0.5 OG samples almost coincide with each other. The behavior of the anodic polarization curves for samples with MAO coatings is still somewhat different. Thus, the minimum value of the anodic current density of complete passivation is observed for the sample 0.1 GO with the coating formed in the electrolyte with a graphene oxide concentration of 0.1 g·L^{-1} (Table 4). Unlike steels that corrode in unstirred NaCl solutions with oxygen depolarization, predominantly with cathodic control with the predominant role of oxygen diffusion, titanium and its alloys retain a passive state in them, i.e., there is a predominant anodic control (Figure 8) [39]. The method of electrochemical impedance spectroscopy (EIS) makes it possible to describe the corrosion behavior by physical and mathematical models, which, in particular, are used to study the effect of GO additives on the physicochemical and protective properties of MAO coatings [31]. Figure 9 shows EIS results for different MAO-coated samples obtained at an OCP in 3.5% NaCl solution. The approximation of the EIS data is shown in the diagrams by solid lines.

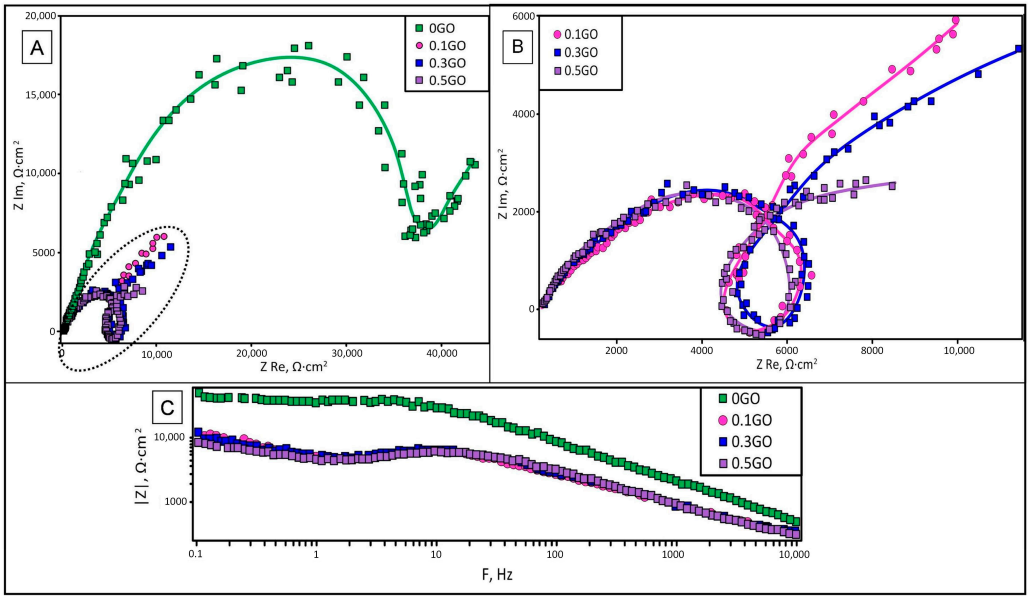

Figure 9. Nyquist plots (**A**), close-up of part of them (**B**), and Bode impedance plots (**C**) obtained in 3.5% NaCl solution for different MAO-coated samples.

It can be seen that closed loops are observed in the Nyquist diagrams for MAO coatings formed in electrolytes with additives of graphene oxide (Figure 9A,B). These dependencies are nontrivial compared to those previously known—for example, [31]—that require the equivalent circuits to be significantly more complicated. The Bode impedance diagrams (Figure 9C) show that the difference in |Z| between the curves for MAO coatings formed in electrolytes with different concentrations of graphene oxide does not exceed 5%. The frequency range for these coatings, which is responsible for the appearance of loops, coincides and is in the range of 0.7–16 Hz. Based on these data, it can be assumed that the degree of filling of the coating pores with graphene oxide for the range of GO concentrations in the electrolyte of 0.1–0.5 g L^{-1} is approximately the same. It should also be noted that in the entire studied frequency range (10^{-1}–10^{4} Hz), the values of the impedance |Z| for MAO coatings formed in electrolytes with additives of graphene oxide are lower than for the 0 GO sample (Figure 9C). This is apparently due to the presence of highly conductive reduced graphene oxide in the pores of the outer layer of these coatings (Figure 5). Graphene oxide, which is a dielectric [40], can be reduced to graphene by photochemical and chemical methods [41], as well as thermally [42]. It can also be assumed that during the anode–cathode MAO, as a result of cathodic polarization and plasma-chemical reactions occurring in the discharge (pore) channels at relatively high temperatures, graphene oxide in the pores of the coating can also be partially reduced. Equivalent circuit elements used to model EIS data typically consist of a combination of resistors (R), inductors (L), capacitances (C), or constant-phase elements (CPE). CPE is preferable to pure capacitance C in the equivalent circuit in terms of modeling EIS data for MAO coatings, which have a non-uniform structure and, consequently, non-ideal capacitance characteristics [43]. The impedance of capacitive constant-phase elements Z_{CPE} can be calculated:

$$Z_{CPE} = n/(j\omega T), \quad (1)$$

where j is the imaginary unit; $\omega = 2\pi F$ is the angular frequency; F is the EIS frequency; T is the capacity of the CPE; n is an empirical constant whose value ranges from 0 to 1. CPE corresponds to an ideal capacitor when the value of n is 1 and the value 0 corresponds to an ideal resistor [44]. The value of n depends on the inhomogeneity of the structure of MAO coatings and the morphology of their surface. The inductance impedance ZL can be calculated:

$$Z_L = j\omega L. \quad (2)$$

Figure 10 shows the equivalent circuits proposed based on the fitted results of EIS for samples with MAO coatings formed on titanium alloy in electrolytes without and with GO additives.

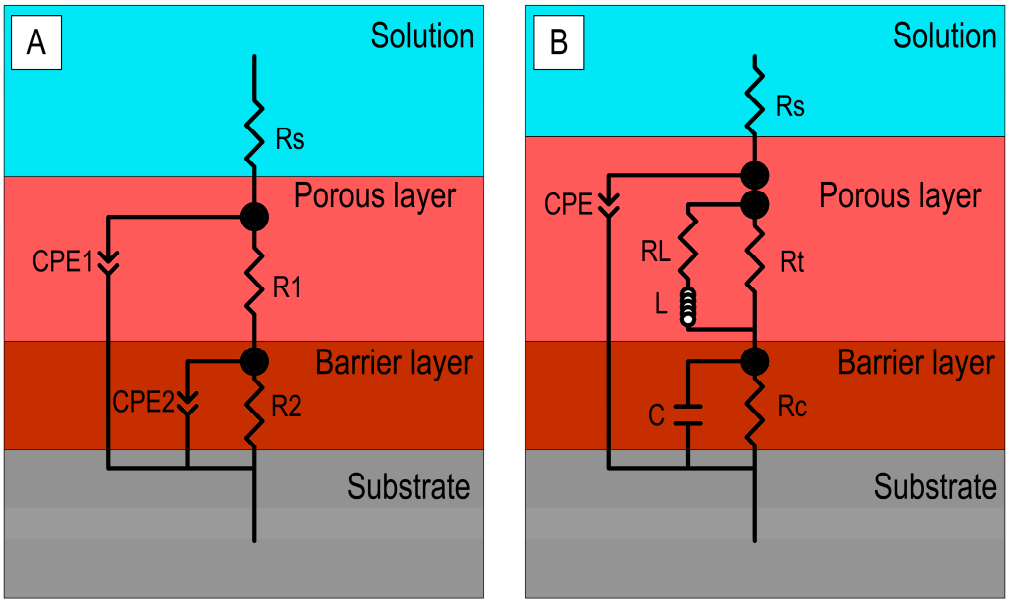

Figure 10. Equivalent circuits proposed based on the fitted results of EIS for samples with MAO coatings formed on titanium alloy in electrolytes without (**A**) and with (**B**) GO additives.

The elements of the equivalent circuit simulating an MAO coating formed on titanium alloy in the base electrolyte without GO additives (Figure 10A) are: Rs is the resistance of 3.5% NaCl solution; R1 and CPE1 are the resistor and the constant-phase element, respectively, corresponding to the outer porous layer of the MAO coating; R2 and CPE2 are the resistor and the constant-phase element, respectively, corresponding to the dense barrier layer of the MAO coating. The elements of the equivalent circuit simulating the MAO coating formed in electrolytes with GO additives (Figure 10B) are: Rs is the resistance of 3.5% NaCl solution; Rt is the resistance of the outer porous layer; RL and L are the resistance and inductance, respectively, associated with the presence of graphene oxide (including partially reduced) inside the pores; Rc is the resistance of the dense barrier layer; C is the capacitance of the electrical double layer at the substrate–coating interface; CPE is constant-phase element corresponding to the entire oxide layer of the MAO coating. It can be seen that in addition to the standard R–CPE units responsible for the outer porous and dense barrier (at the boundary with the metal substrate) layers of the MAO coating (Figure 10A), in the case of coatings formed in electrolytes with the oxide graphene additives (Figure 10B), to describe the loops in the Nyquist diagram (Figure 9B), the resistor RL and the inductance L are introduced into the equivalent circuit, which is due to the presence of graphene oxide (including partially reduced) inside the pores (Figure 5). The values of the parameters of equivalent circuit elements (Figure 10), proposed based on the fitted results of EIS, for samples with MAO coatings formed on titanium alloy in electrolytes without and with GO additives, are presented in Table 5.

Table 5. The value of the parameters of equivalent circuit elements for samples with MAO coatings formed on titanium alloy in electrolytes without (0 GO) and with (With GO) graphene oxide additives.

Sample	Rs, Ω	R1, Ω	CPE1		R2, Ω	CPE2		Error, %
			T, F	*n*		T, F	*n*	
0 GO	33	$4.2 \cdot 10^{3}$	$8.1 \cdot 10^{-6}$	0.76	$2.2 \cdot 10^{19}$	$1.3 \cdot 10^{-4}$	0.92	7.1
Samples	**Rt, Ω**	**RL, Ω**	**L, H**	**Rc, Ω**	**C, F**	**CPE**		**Error, %**
						T, F	*n*	
With GO	$2.2 \cdot 10^{3}$	$8.4 \cdot 10^{2}$	27	$4.4 \cdot 10^{3}$	$9.4\ 10^{-4}$	$1.6\ 10^{-4}$	0.48	7.1

It can be seen that the resistance R2 of the dense barrier layer of the MAO coating formed on titanium alloy in the base electrolyte without GO additives is many orders of magnitude higher than the resistance R1 of the outer porous layer filled with 3.5% NaCl solution. A dense barrier layer adjacent to the metal substrate and responsible for the corrosion-protective ability of the coating consists of rutile and anatase (Figure 6). The outer porous layer apparently consists of X-ray amorphous silicon dioxide and titanosilicates, as there are no silicon-containing phases on the X-ray diffraction patterns (Figure 6), and in the elemental profile of the coating in this area, silicon is the dominant element (Figure 3). Although the impedance |Z| for coatings formed in electrolytes with graphene oxide additives is lower than for the 0 GO sample (Figure 9C), which may be due to the anode–cathode MAO mode used in this work (in contrast to [31]) and, as a consequence, the partial reduction of GO in pore coatings, at low frequencies, there is the tendency to significantly increase the impedance for them, especially for the 0.1 GO sample (Figure 9C).

Electrochemical polarization studies also showed that the minimum value of the anodic current density of complete passivation is observed for the 0.1 GO sample (Figure 8, Table 4). Increasing the concentration of graphene oxide in the electrolyte to more than 0.1 $g \cdot L^{-1}$ does not improve the protective properties of the coatings.

4. Conclusions

MAO coatings with a thickness from ~40 to ~50 µm were obtained in silicate-hypophosphite electrolytes with graphene oxide additives on samples of titanium alloy Ti6Al4V. With an increase in the content of graphene oxide in the electrolyte from 0 to 0.5 $g \cdot L^{-1}$, its pH slightly decreases, while the conductivity of the electrolyte increases by about 1.5 times. With an increase in the content of graphene oxide in the electrolyte from 0 to 0.1 g L^{-1}, the thickness of the coatings increases by about 20%, and with a further increase in the concentration of GO from 0.1 to 0.5 $g \cdot L^{-1}$, a very slight increase in the thickness of the coatings occurs. The roughness of MAO coatings also approximately doubles when $g \cdot L^{-1}$ GO is inputted into the electrolyte, but with a further increase in the concentration of graphene oxide in the electrolyte, it almost does not increase. The input of graphene oxide additives into the base silicate-hypophosphite electrolyte leads to an increase in the hardness of MAO coatings from 331 to 366 HV with an increase in the GO concentration from 0.1 to 0.5 $g \cdot L^{-1}$. Electrochemical polarization studies in 3.5% NaCl corrosive solution and impedance data showed that the best characteristics in terms of corrosion-protective ability among coatings formed in electrolytes with GO additives are those formed in the electrolyte with a GO concentration of 0.1 $g \cdot L^{-1}$. A further increase in the GO concentration in the electrolyte does not improve the protective properties of MAO coatings.

Author Contributions: Conceptualization, S.G. and P.P.; methodology, N.K., A.A. and A.Z.; software, N.P. and E.K.; validation, A.Z. and M.G.; formal analysis, A.R. and E.K.; investigation, A.S. and M.G.; resources, O.Y. and P.P.; data curation, S.G. and M.V.; writing—original draft preparation, N.P., M.G. and A.A.; writing—review and editing, A.A. and A.S.; visualization, N.P. and A.R.; supervision, O.Y. and P.P.; project administration, N.K. and M.V.; funding acquisition, O.Y. and A.S. All authors have read and agreed to the published version of the manuscript.

Funding: This work is funded by the state assignment of the Ministry of Science and Higher Education of the Russian Federation, Project No FSFS-2021-0006.

Data Availability Statement: Not applicable.

Acknowledgments: The work was carried out on the equipment of the Collective Use Center of MSTU "STANKIN" (project No. 075-15-2021-695).

Conflicts of Interest: The authors declare no conflict of interest.

References

1. Prasad, S.; Ehrensberger, M.; Gibson, M.P.; Kim, H.; Monaco, E.A., Jr. Biomaterial properties of titanium dentistry. *J. Oral Biosci.* **2015**, *57*, 192–199. [CrossRef]
2. Kaur, M.; Singh, K. Review on titanium and titanium based alloys as biomaterials for orthopaedic applications. *Mater. Sci. Eng. C* **2019**, *102*, 844–862. [CrossRef] [PubMed]
3. Sieniawski, J.; Filip, R.; Ziaja, W. The effect of microstructure on the mechanical properties of two-phase titanium alloys. *J. Mater. Process. Technol.* **2003**, *133*, 84–89. [CrossRef]
4. Lei, Z.; Gao, P.; Wang, X.; Zhan, M.; Li, H. Analysis of anisotropy mechanism in the mechanical property of titanium alloy tube formed through hot flow forming. *J. Mater. Sci. Technol.* **2021**, *86*, 77–90. [CrossRef]
5. Ferraris, S.; Spriano, S. Porous Titanium by Additive Manufacturing: A Focus on Surfaces for Bone Integration. *Metals* **2021**, *11*, 1343. [CrossRef]
6. Volosova, M.A.; Grigoriev, S.N.; Kuzin, V.V. Effect of Titanium Nitride Coating on Stress Structural Inhomogeneity in Oxide-Carbide Ceramic. Part 4. Action of Heat Flow. *Refract. Ind. Ceram.* **2015**, *56*, 91–96. [CrossRef]
7. Li, Y.; Zhou, Q.; Liu, M. Effect of novel surface treatment on corrosion behavior and mechanical properties of a titanium alloy. *Baosteel Tech. Res.* **2021**, *15*, 11–19.
8. Smurov, I.; Doubenskaia, M.; Grigoriev, S.; Nazarov, A. Optical Monitoring in Laser Cladding of Ti6Al4V. *J. Therm. Spray Technol.* **2012**, *21*, 1357–1362. [CrossRef]
9. Li, J.; Wang, Y.; Yao, Y.; Wang, Y.; Wang, L. Structure and tribological properties of TiSiCN coating on Ti6Al4V by arc ion plating. *Thin Solid Films* **2017**, *644*, 115–119. [CrossRef]
10. Metel, A.; Bolbukov, V.; Volosova, M.; Grigoriev, S.; Melnik, Y. Equipment for deposition of thin metallic films bombarded by fast argon atoms. *Instrum. Exp. Tech.* **2014**, *57*, 345–351. [CrossRef]
11. Wang, P.; Xu, Z.; Liu, X.; Wang, H.; Qin, B.; Lin, J.; Cao, J.; Qi, J.; Feng, J. Regulating the interfacial reaction of $Sc_2W_3O_{12}$/AgCuTi composite filler by introducing a carbon barrier layer. *Carbon* **2022**, *191*, 290–300. [CrossRef]
12. Kumar, D.; Pandey, K.K.; Kumari, S.; Nair, A.M.; Mirche, K.K.; Maurya, S.S.; Pandey, S.M.; Keshri, A.K. Effect of nanodiamond concentration on the electrochemical behavior of plasma sprayed titanium-nanodiamond nanocomposite coatings. *Diam. Relat. Mater.* **2022**, *130*, 109419. [CrossRef]
13. Grigoriev, S.; Peretyagin, N.; Apelfeld, A.; Smirnov, A.; Yanushevich, O.; Krikheli, N.; Kramar, O.; Kramar, S.; Peretyagin, P. Investigation of MAO Coatings Characteristics on Titanium Products Obtained by EBM Method Using Additive Manufacturing. *Materials* **2022**, *15*, 4535. [CrossRef]
14. Apelfeld, A.V.; Belkin, P.N.; Borisov, A.M.; Vasin, V.A.; Krit, B.L.; Ludin, V.B.; Somov, O.V.; Sorokin, V.A.; Suminov, I.V.; Frantskevich, V.P. Modern technologies for modification of materials surface and formation of protective coatings. In *Volume 1: Micro-Arc Oxidation*; Renome: Moscow, Russia; St.-Petersburg, Russia, 2017; 648p, ISBN 978-5-91918-832-2.
15. Grigoriev, S.; Pristinskiy, Y.; Volosova, M.; Fedorov, S.; Okunkova, A.; Peretyagin, P.; Smirnov, A. Wire Electrical Discharge Machining, Mechanical and Tribological Performance of TiN Reinforced Multiscale SiAlON Ceramic Composites Fabricated by Spark Plasma Sintering. *Appl. Sci.* **2021**, *11*, 657. [CrossRef]
16. Borisov, A.M.; Krit, B.L.; Lyudin, V.B.; Morozova, N.V.; Suminov, I.V.; Apelfeld, A.V. Microarc oxidation in slurry electrolytes: A review. *Surf. Eng. Appl. Electrochem.* **2016**, *52*, 50–78. [CrossRef]
17. Podrabinnik, P.; Gershman, I.; Mironov, A.; Kuznetsova, E.; Peretyagin, P. Mechanisms involed in the formation of secondary structures on the friction surface of experimental aluminium alloys for monometallic journal bearings. *Lubricants* **2018**, *6*, 104. [CrossRef]
18. Diaz, L.A.; Montes-Moran, M.A.; Peretyagin, P.Y.; Vladimirov, Y.G.; Okunkova, A.; Moya, J.S.; Torrecillas, R. Zirconia-alumina-nanodiamond composites with gemological properties. *J. Nanopart. Res.* **2014**, *16*, 2257. [CrossRef]
19. Guo, Y.; Xu, L.; Luan, J.; Wan, Y.; Li, R. Effect of carbon nanotubes additive on tribocorrosion performance of micro-arc oxidized coatings on Ti6Al4V alloy. *Surf. Interfaces* **2022**, *28*, 101626. [CrossRef]
20. Bogdashkina, N.L.; Gerasimov, M.V.; Zalavutdinov, R.K.; Kasatkina, I.V.; Krit, B.L.; Lyudin, V.B.; Fedichkin, I.D.; Shcherbakov, A.I.; Apelfeld, A.V. Influence of Nickel Sulfate Additives to Electrolytes Subjected to Microarc Oxidation on the Structure, Composition and Properties of Coatings Formed on Titanium. *Surf. Eng. Appl. Electrochem.* **2018**, *54*, 331–337. [CrossRef]
21. Smirnov, A.; Seleznev, A.; Solis Pinargote, N.W.; Pristinskiy, Y.; Peretyagin, P.; Bartolome, J.F. The Influence of Wire Electrical Discharge Machining Cutting Parameters on the Surface Roughness and Flexural Strength of ZrO_2/TiN Ceramic Nanocomposites Obtained by Spark Plasma Sintering. *Nanomaterials* **2019**, *9*, 1391. [CrossRef]

22. Shokouhfar, M.; Allahkaram, S. Effect of incorporation of nanoparticles with different composition on wear and corrosion behavior of ceramic coatings developed on pure titanium by micro arc oxidation. *Surf. Coat. Technol.* **2017**, *309*, 767–778. [CrossRef]
23. Zhao, D.; Lu, Y.; Zeng, X.; Wang, Z.; Liu, S.; Wang, T. Antifouling property of micro-arc oxidation coating incorporating Cu_2O nanoparticles on Ti6Al4V. *Surf. Eng.* **2017**, *33*, 796–802. [CrossRef]
24. Li, H.; Sun, Y.; Zhang, J. Effect of ZrO_2 particle on the performance of micro-arc oxidation coatings on Ti6Al4V. *Appl. Surf. Sci.* **2015**, *342*, 183–190. [CrossRef]
25. Chen, Q.; Jiang, Z.; Tang, S.; Dong, W.; Tong, Q.; Li, W. Influence of graphene particles on the micro-arc oxidation behaviors of 6063 aluminum alloy and the coating properties. *Appl. Surf. Sci.* **2017**, *423*, 939–950. [CrossRef]
26. Gao, Y.; Yang, W.; Xu, D.; Chetn, J.; Jialng, B. Microstructure and Properties of Graphene Oxide-doped TiO_2 Coating on Titanium by Micro Arc Oxidation. *J. Wuhan Univ. Technol.-Mater. Sci. Edit.* **2018**, *33*, 1524–1529. [CrossRef]
27. Wen, C.; Zhan, X.; Huang, X.; Xu, F.; Luo, L.; Xia, C. Characterization and corrosion properties of hydroxyapatite/graphene oxide bio-composite coating on magnesium alloy by one-step micro-arc oxidation method. *Surf. Coat. Technol.* **2017**, *317*, 125–133. [CrossRef]
28. Li, Z.; Cai, Z.; Ding, Y.; Cui, X.; Yang, Z.; Zhu, M. Characterization of graphene oxide/ZrO_2 composite coatings deposited on zirconium alloy by micro-arc oxidation. *Appl. Surf. Sci.* **2020**, *506*, 144928. [CrossRef]
29. Zhang, Y.; Chen, F.; Zhang, Y.; Liu, Z.; Wang, X.; Du, C. Influence of graphene oxide on the antiwear and antifriction performance of MAO coating fabricated on MgLi alloy. *Surf. Coat. Technol.* **2019**, *364*, 144–156. [CrossRef]
30. Askarnia, R.; Roueini Fardi, S.; Sobhani, M.; Staji, H.; Aghamohammadi, H. Effect of graphene oxide on properties of AZ91 magnesium alloys coating developed by micro-arc oxidation process. *J. Alloys Compd.* **2022**, *892*, 162106. [CrossRef]
31. Wang, J.; Liu, L.; Yang, M.; Wu, X.; Li, S.; Zhang, W.; Zhang, H. Modification effect of graphene oxide on oxidation coating of Ti-3Zr-2Sn-3Mo-25 Nb near-β titanium alloy. *J. Alloys Compd.* **2022**, *901*, 163561. [CrossRef]
32. Grigoriev, S.; Smirnov, A.; Solis Pinargote, N.W.; Yanushevich, O.; Kriheli, N.; Kramar, O.; Pristinskiy, Y.; Peretyagin, P. Evaluation of Mechanical and Electrical Performance of Aging Resistance ZTA Composites Reinforced with Graphene Oxide Consolidated by SPS. *Materials* **2022**, *15*, 2149. [CrossRef]
33. Smirnov, A.; Peretyagin, P.; Bartolomé, J.F. Processing and mechanical properties of new hierarchical metal-graphene flakes reinforced ceramic matrix composites. *J. Eur. Ceram. Soc.* **2019**, *39*, 3491–3497. [CrossRef]
34. Hummers, W.S., Jr.; Offeman, R.E. Preparation of graphitic oxide. *J. Am. Chem. Soc.* **1958**, *80*, 1339. [CrossRef]
35. Zuo, Y.; Li, T.; Yu, P.; Zhao, Z.; Chen, X.; Zhang, Y.; Chen, F. Effect of graphene oxide additive on tribocorrosion behavior of MAO coatings prepared on Ti6Al4V alloy. *Appl. Surf. Sci.* **2019**, *480*, 26−34. [CrossRef]
36. Shcherbakov, A.I.; Korosteleva, I.G.; Kasatkina, I.V.; Kasatkin, V.E.; Kornienko, L.P.; Dorofeeva, V.N.; Vysotskii, V.V.; Kotenev, V.A. Impedance of an Aluminum Electrode with a Nanoporous Oxide. *Prot. Met. Phys. Chem. Surf.* **2019**, *55*, 689–694. [CrossRef]
37. Ullmann, F. *Chemical Encyclopedia*; Soviet Encyclopedia: Moscow, Russia, 1988; Volume 4, p. 1176.
38. Yan, Y.; Liu, T.; Lin, J.; Qiao, L.; Tu, J.; Qin, S.; Cao, J.; Qi, J. Interaction between the third alloying element and the interfacial structure of AgCu-alloy brazed heterogeneous metal integration. *J. Alloys Compd.* **2021**, *883*, 160933. [CrossRef]
39. Tomashov, N.D.; Chernova, G.P. *Theory of Corrosion and Corrosion-Resistant Constructional Alloys*; Metallurgy: Moscow, Russia, 1993; 413p, ISBN 5-229-00923-3.
40. Gómez-Navarro, C.; Weitz, R.T.; Bittner, A.M.; Scolari, M.; Mews, A.; Burghard, M.; Kern, K. Electronic transport properties of individual chemically reduced graphene oxide sheets. *Nano Lett.* **2007**, *7*, 3499–3503. [CrossRef]
41. Shulga, M.Y.; Shulga, Y.N.; Parkhomenko, N.Y. Carbon nanostructures reduced from graphite oxide as electrode materials for supercapacitors. *Mod. Electron. Mater.* **2015**, *1*, 157.
42. Neustroev, E.P.; Nogovitsyna, M.V.; Solovieva, Y.u.S.; Aleksandrov, G.N.; Burtseva, E.K. Study of the electrical conductivity of thermally reduced graphene oxide. *Nanosystems* **2015**, *7*, 162–167. [CrossRef]
43. Mashtalyar, D.V.; Gnedenkov, S.V.; Sinebryukhov, S.L.; Imshinetskiy, I.M.; Puz', A.V. Plasma electrolytic oxidation of the magnesium alloy MA8 in electrolytes containing TiN nanoparticles. *J. Mater. Sci. Technol.* **2017**, *33*, 461–468. [CrossRef]
44. Pezzato, L.; Angelini, V.; Brunelli, K.; Martini, C.; Dabalà, M. Tribological and corrosion behavior of PEO coatings with graphite nanoparticles on AZ91 and AZ80 magnesium alloys. *Trans. Nonferrous Metal. Soc. China* **2018**, *28*, 259–272. [CrossRef]